Detection of Human Influence on Trends of North Atlantic Ocean Wave Heights and Atmospheric Storminess

Xiaolan L. Wang, Val. R. Swail, Xuebin Zhang, Francis W. Zwiers
Climate Research Division, ASTD, STB, Environment Canada

Myles Allen
Department of Physics, University of Oxford

1. Introduction

After the 2005 disaster of hurricane Katrina and the tsunami tragedy that struck Asia in the end of 2004, the public awareness of the potential impacts of storm surges and ocean waves on the human society, environment and ecosystem has increased. One of the issues of concern is whether or not there exists human influence on the storm and ocean wave climate. Although this issue is yet to be addressed (and we attempt to do so in this study), there is evidence for significant changes in North Atlantic cyclone activity and ocean wave heights in the cold seasons of the last half century. For example, a significant increasing trend in winter (January-March) strong-cyclone activity over the high-latitude North Atlantic has been identified in the sea level pressure (SLP) fields taken from both the ERA40 reanalysis (ERA40 hereafter; Uppala et al., 2005) and the NCEP-NCAR Reanalysis (NNR hereafter; Kalnay et al., 1996; Kistler et al., 2001) for the 1958-2001 period, which also show a significant decreasing trend over the mid-latitude North Atlantic (Wang et al., 2006). These changes are found to be associated with the mean position of the North Atlantic storm track shifting about 181 km northward (Wang et al., 2006). Consistent with such cyclone activity trends is that the northeast North Atlantic ocean was found to have roughened in winter during the 1958-1997 period, while significant decreases of ocean wave heights are identified in the subtropical North Atlantic (Wang and Swail, 2006a; Wang and Swail, 2002 and 2001; WASA Group, 1998; Bacon and Carter, 1991). In this study, we detect human influence on the storm and ocean wave climate, on the basis of multiple climate model simulations of human-induced climate change and statistical simulations of the corresponding changes in ocean wave heights.

2. Data, detection method, and results

Since ocean wave heights are not directly available from the output of global climate models, we use a statistical model to represent the observed relationship between the atmosphere and significant wave height (SWH), which is in turn used to simulate the SWH changes corresponding to climate model simulations of human-induced climate change. It has been shown that seasonal mean SLP anomalies, P_t, and seasonal mean anomalies of squared SLP gradients, G_t, are good predictors for ocean wave heights (Wang and Swail, 2006a and 2006b). Thus, statistical simulations of SWH changes corresponding to the simulated global warming are conducted in the same way as in Wang and Swail (2006b), using the following regression model:

$$X_t = a + bP_t + cG_t + e_t, \qquad (1)$$

where X_t denotes either seasonal mean SWH, H_t, or the time-dependent location parameter, m_t, of the generalized extreme value distribution, $GEV(m_t, s, x)$, of seasonal maximal SWH, and e_t denotes a white noise process.

For each year t, we calculate P_t and G_t from the relevant monthly mean SLP fields taken from ERA40 and NNR for the 1958-2001 period and use them as proxy of observations. For both

P_t and G_t, the anomalies are relative to its climate of the baseline period 1961-1990, and are on a 5°×5° lat-long grid. As proxy of SWH observations, we use seasonal means and maxima of SWH derived from the original ERA40 wave data (Uppala et al, 2005; Caires et al., 2004), which are on the same 5°×5° lat-long grid as do P_t and G_t and are hereafter referred to as "observed" wave data. Two seasons are analyzed here, that is, winter (January-March or JFM) and fall (October-December or OND). Further, the climate model simulated P_t and G_t are derived from nine ensembles of integrations (45 in total) with historical greenhouse gases and sulphate aerosols forcing from nine coupled ocean-atmosphere models (see Table 1), which were obtained from the IPCC Fourth Assessment Report (AR4) model output archive.

Table 1. The nine coupled ocean-atmosphere models used in this study and the number of integrations (runs) conducted with each of these models.

Model	Number of runs
ECHO-G	5
GFDL CM2.0	3
GFDL CM2.1	3
GISS Model E H	5
GISS Model E R	9
MIROC 2 medres	3
MRI CGCM2 3 2a	5
NCAR CCSM 3	8
NCAR PCM 1	4

First, the above regression relationships are trained using detrended series of the related SWH and SLP variables for the 44-year period from 1958-2001, so that the effect of trends in the time series of the predictand and predictors on the relationship is diminished. Such SWH-SLP relationships are then used to simulate seasonal means and 20-yr return values of SWH that correspond to climate model simulations of human-induced climate change, by feeding the climate model simulated P_t and G_t into the estimated regression relationship $\hat{H}_t = \hat{a} + \hat{b}P_t + \hat{c}G_t$ or $GEV(\hat{\boldsymbol{m}}_t = \hat{a} + \hat{b}P_t + \hat{c}G_t, \hat{\boldsymbol{s}}, \hat{\boldsymbol{x}})$. Such simulations are conducted for each of the 45 integrations of human-induced climate change, subsequently. Further, in order to have a set of SWH "observations" that are somewhat independent of the model used for ERA40, we also feed the P_t and G_t as derived from NNR to the regression relationship, to obtain the related (statistical) hindcasts of the SWH variables for the 1958-1999 period (hereafter referred to as the NNR hindcast of SWH; note that an original NNR wave dataset does not exist). For comparison, an ERA40 hindcast of the SWH variables for the same 42-year period is also obtained, using P_t and G_t as derived from ERA40.

Then, a linear trend is estimated for each of the "observed"/hindcast and simulated SWH variables (seasonal mean anomalies and 20-yr return values of SWH, H_{avg} and H_{20y}) at each grid point for the 42-year period from 1958 to 1999 (because the climate model integrations do not cover the period after 1999). The resulting observed/hindcast trend patterns are compared with the corresponding multi-model mean trend patterns to determine whether or not human influence on the observed trend pattern is detectable. More specifically, we take the optimal detection approach (Allen and Stott, 2003), which assumes that the observed linear trends (Y_o) may be represented as the linear sum of the scaled simulated response (Y_m) to greenhouse gas and sulphate aerosol forcing, and the internal variability ($\boldsymbol{h}$) in the observed trends:

$$Y_o = b(Y_m - V) + h \qquad (2)$$

where V denotes the component of internal variability in the simulated response to greenhouse gas and sulphate aerosol forcing (i.e., in the mutli-model mean trends). It is also assumed that V and h share the same structure. The regression coefficient b is estimated with a total least-squares fit, with its uncertainty range being estimated from the inter-integration variability (after removing the ensemble mean field from each integration in that ensemble). The forcing response pattern is detected if b is found to be positive and inconsistent with zero. We also check whether the climate models provide a plausible explanation of the observations by testing whether or not the residual h is consistent with the corresponding inter-integration variability, which is estimated using the climate model simulations for 1900-1941 (a period different from the period used for estimates of trends and b).

While human influence on SLP (i.e., equivalent of P_t) has been detected (Gillett et al., 2003), work on detection of human influence on G_t, which represents the field of geostraphic wind energy and hence the atmospheric storminess, has not been done. Thus, the same optimal detection approach is also applied to detect human influence on the trend patterns of P_t and G_t, separately, using the quantities derived from either ERA40 or NNR as proxy of observations.

Figure 1 shows the estimated linear trend patterns of P_t as derived from ERA40, NNR, and the multi-model/ensemble mean simulations of P_t, respectively. These patterns are in agreement with those shown in (Gillett et al., 2003). Generally, they are characterized by a downward trend in the high-latitudes and an upward trend in the mid-latitudes, with the zero-trend contour locating more southward in fall than in winter (compare the right and left panels in Fig. 1). The multi-model simulated trend patterns are very similar to the observed ones as derived from either ERA40 or NNR, especially in winter, although the magnitude of trend is generally underestimated by the climate models. There is little difference between ERA40 and NNR, except that ERA40 shows larger trends than does NNR, especially in fall (see Figs. 1a-b and 1e-f).

As shown in Fig. 2, the trend patterns of G_t are characterized by a strong upward trend in the high-latitudes and a relatively weaker downward trend to its south, with the center of the upward trend locating a little more southward and less zonally-oriented than that of the corresponding P_t trend pattern. The differences of trend magnitude between winter and fall are also more prominent for G_t than for P_t (Figs. 1 and 2). There is no remarkable difference between ERA40 and NNR in terms of the trend pattern of G_t. Note that the storminess trends as inferred from the geostraphic wind energy (G_t) field are also consistent with the findings of previous studies using different storminess indices (e.g., Wang et al. 2006).

Figure 3 shows the estimated linear trend patterns of seasonal means and 20-year return values of SWH (H_{avg} and H_{20y}) as derived from the original ERA40 wave data, the NNR hindcast wave data, and the multi-model/ensemble mean simulations of H_{avg} and H_{20y}, respectively. The trend patterns as derived from the ERA40 hindcast wave data are not shown here, because they are very similar to those shown in Figs. 3e-f and 3k-l. In winter, the trend patterns are characterized by an upward trend in the northeast North Atlantic and a downward trend in the mid-latitudes, with little difference between the observed and simulated trend patterns (except that the simulated magnitude of trend is much smaller than the observed one). In fall, the center of the upward trend in the ERA40 wave data is more meridian-oriented and centered in the North Atlantic than the corresponding simulated one, with more profound differences between the observed and simulated trend patterns for the extreme wave heights (compare Figs. 3b,d and

3h,j), especially in the northeast North Atlantic. In general, the extreme wave heights seem to have larger trends than do the seasonal means, especially in the original ERA40 wave data.
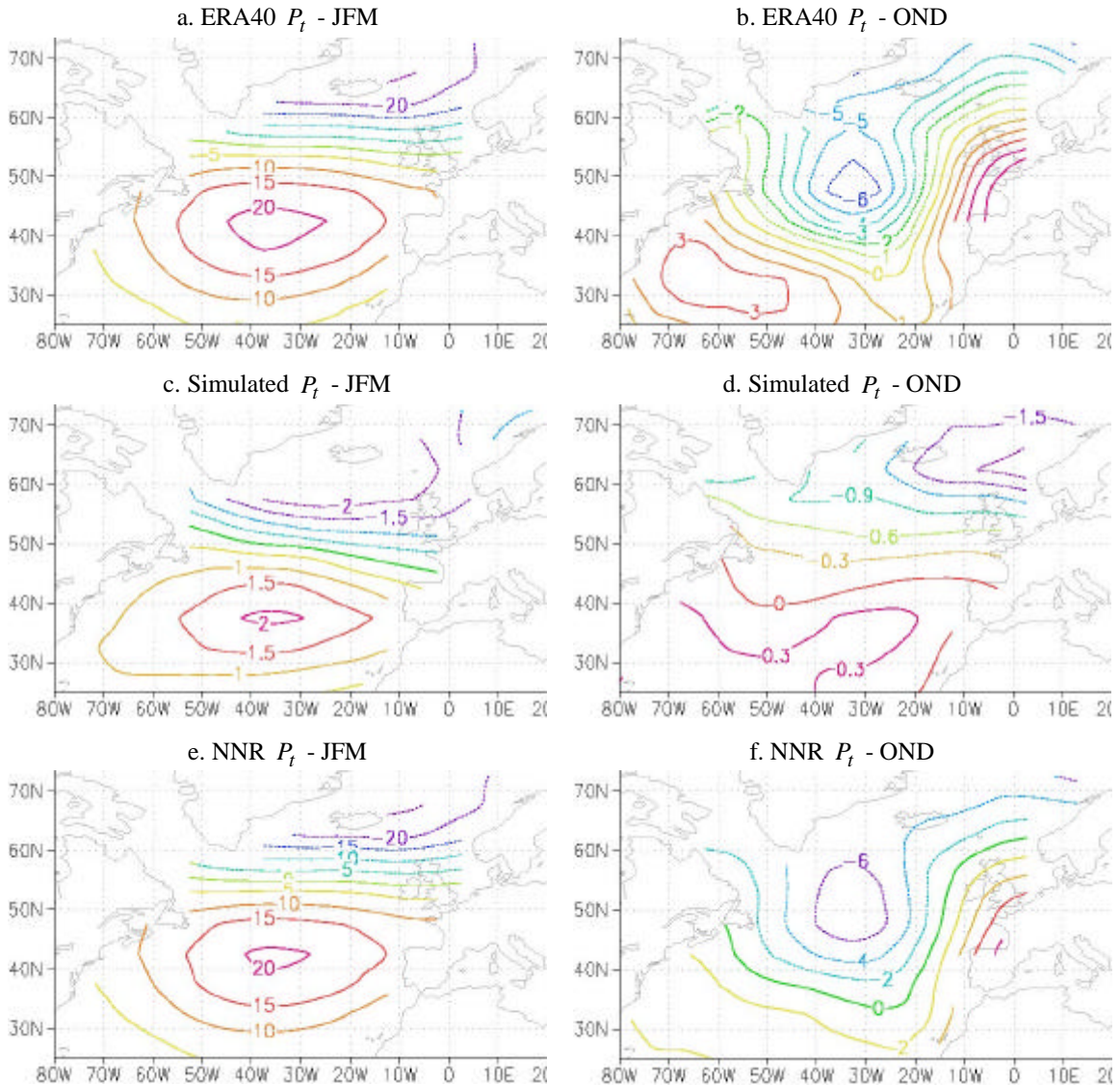
a. ERA40 P_t - JFM

b. ERA40 P_t - OND

c. Simulated P_t - JFM

d. Simulated P_t - OND

e. NNR P_t - JFM

f. NNR P_t - OND

Figure 1. The 1958-1999 trend patterns of the seasonal mean SLP anomalies (P_t) as derived from ERA40, NNR, and the multi-model/ensemble mean simulations of P_t. Solid contours indicate upward/positive trends, and dashed ones downward/negative trends. Note the different scales of contour levels, i.e., the simulated trends (panels c-d) are smaller than those of ERA40 or NNR, as indicated by the contour labels.
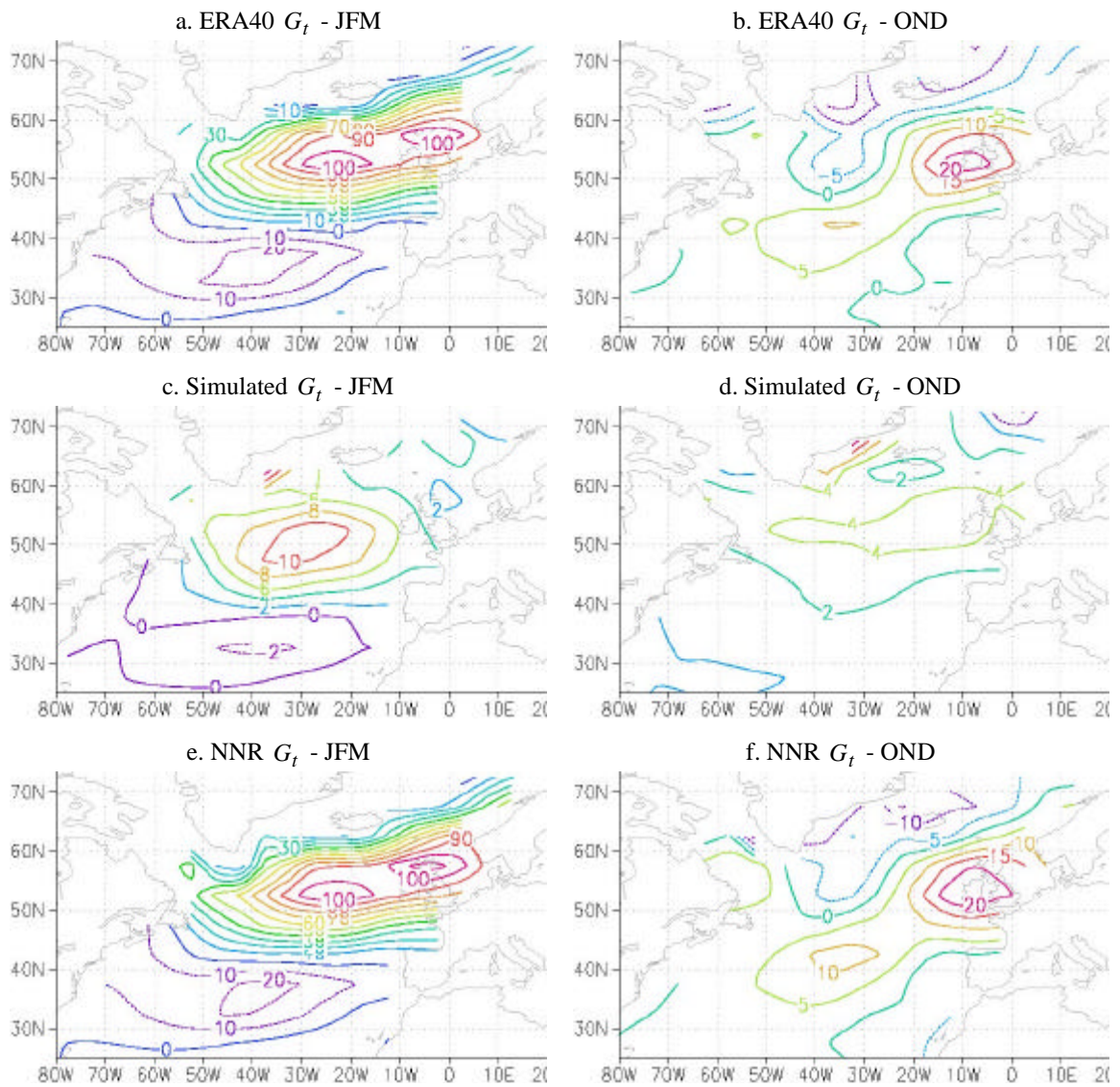
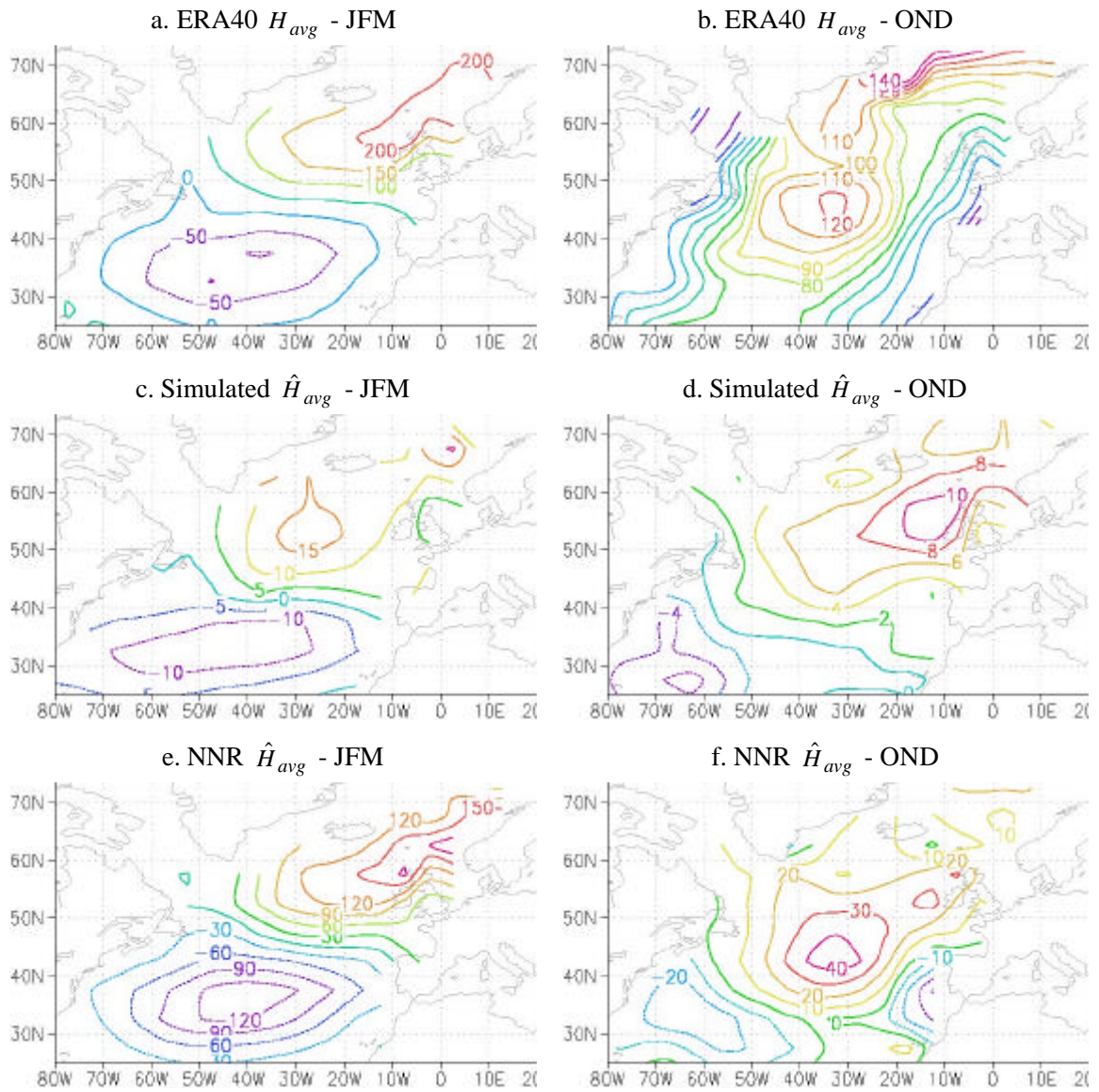**Figure 2.** The same as in Fig. 1 but for the 1958-1999 trend patterns of seasonal anomalies of squared SLP gradient (G_t).

a. ERA40 H_{avg} - JFM

b. ERA40 H_{avg} - OND

c. Simulated $\hat{H}_{avg}$ - JFM

d. Simulated $\hat{H}_{avg}$ - OND

e. NNR $\hat{H}_{avg}$ - JFM

f. NNR $\hat{H}_{avg}$ - OND

Figure 3. The same as in Fig. 1 but for the 1958-1999 trend patterns of the seasonal means and 20-year return values of SWH, H_{avg} and H_{20y}, as derived from the original ERA40 wave data, the NNR hindcast wave data, and the multi-model/ensemble mean simulations of H_{avg} and H_{20y} (i.e., $\hat{H}_{avg}$ and $\hat{H}_{20y}$), respectively.

g. ERA40 H_{20y} - JFM

h. ERA40 H_{20y} - OND

i. Simulated $\hat{H}_{20y}$ - JFM

j. Simulated $\hat{H}_{20y}$ - OND

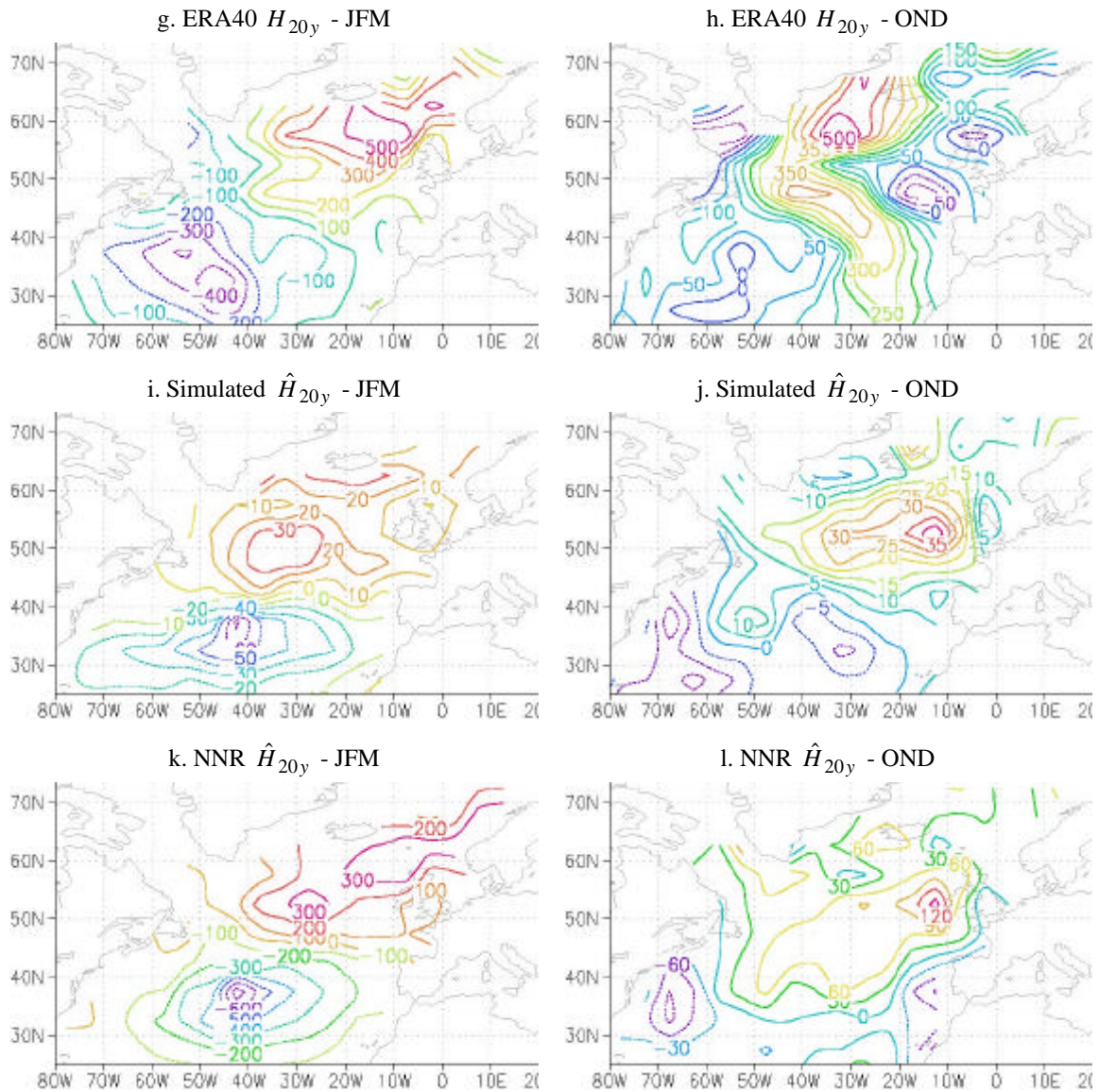k. NNR $\hat{H}_{20y}$ - JFM

l. NNR $\hat{H}_{20y}$ - OND

Figure 3. (Continued)

As summarized in Table 2 and shown in Fig. 4, results of our detection study indicate that there exist detectable human influences on the observed 1958-1999 trends of North Atlantic ocean wave heights and storminess, because the scaling factor **b** was found to be significantly greater than zero (i.e., inconsistent with zero) in each case (Fig. 4). These results are consistent with the relative magnitudes of the responses shown in Figs. 1-3. They are also consistent across the different variables (P_t, G_t, H_{avg}, and H_{20y}) and across the different data sets (ERA40 or NNR, original or hindcast wave data). Moreover, the results of detection on the wave heights are physically consistent with those of detection on the SLP anomalies or on the geostraphic wind energy field. Decreases in SLP and/or increases in geostraphic wind energy are associated with increases in ocean wave heights (both seasonal means and seasonal extremes). For P_t, our results

are in agreement with the findings of Gillett et al. (2003), with the estimated scaling factor ranging from 6.1 to 7.3 (Table 2), although the domain of this study is only the North Atlantic sector while it is global or hemispheric in Gillett et al. (2003).

Table 2. The estimated scaling factor $\hat{b}$, its 5-95% uncertainty range ($\hat{b}_l$, $\hat{b}_h$), and the result of the related residual check for each of the listed detection variables as derived from the ERA40 or NNR dataset. The "#EOFs" column shows the numbers of retained leading EOFs corresponding to these estimates, with the range of EOF truncation that leads to similar results shown in the parentheses. Here, "small V" means that the climate models were found to underestimate the internal variability, which leads to conservative detection conclusions. In the "Residual check" column, the expression in parentheses means that an EOF truncation at the indicated range is associated with "small V".

| Season	Detection variable	$\hat{b}$	$\hat{b}_l$	$\hat{b}_h$	#EOFs	Residual check
JFM	ERA40 P_t	6.250	2.360	15.480	6 (4-7)	OK (others in 2-12:small V)
	ERA40 G_t	4.475	0.684	12.402	13	OK (others but 5:small V)
	ERA40 H_{avg}	11.820	6.036	34.085	2	OK (3-13:small V)
	ERA40 H_{20y}	11.081	5.259	36.272	2	OK (3-9:small V)
	ERA40 $\hat{H}_{avg}$	6.220	2.461	14.741	7 (6-7)	OK (others in 2-9:small V)
	ERA40 $\hat{H}_{20y}$	6.886	3.023	15.991	7 (6-8)	OK (others in 2-11:small V)
	NNR P_t	6.178	2.266	15.516	6 (4-7)	OK (others in 4-12:small V)
	NNR G_t	4.846	0.573	15.662	9 (7-10)	OK (others but 11,13,14:small V)
	NNR $\hat{H}_{avg}$	6.106	2.426	14.213	7 (6-7)	OK (others in 2-9:small V)
	NNR $\hat{H}_{20y}$	6.837	2.952	16.070	6 (2,6-7,9)	OK (others in 2-11:small V)
OND	ERA40 P_t	6.995	3.281	15.310	*19 (7-24)*	small V
	ERA40 G_t	2.687	0.210	6.012	*23 (22-30)*	small V
	ERA40 H_{avg}	13.545	6.963	43.529	2 (2-3)	OK (4-11:small V)
	ERA40 H_{20y}	8.658	3.512	28.665	3 (2-3)	OK (4-7:small V)
	ERA40 $\hat{H}_{avg}$	4.408	0.974	10.885	*10 (14-30)*	small V
	ERA40 $\hat{H}_{20y}$	4.063	1.390	8.197	12 (11-12)	OK (others in 10-23:small V)
	NNR P_t	7.295	3.394	16.570	*19 (6-8,10-20)*	small V
	NNR G_t	2.720	0.027	6.457	18	OK (21-30:small V)
	NNR $\hat{H}_{avg}$	5.038	1.727	11.334	*20 (14-20,23-24)*	small V
	NNR $\hat{H}_{20y}$	4.456	1.789	8.664	12 (10-12)	OK (13-17:small V)
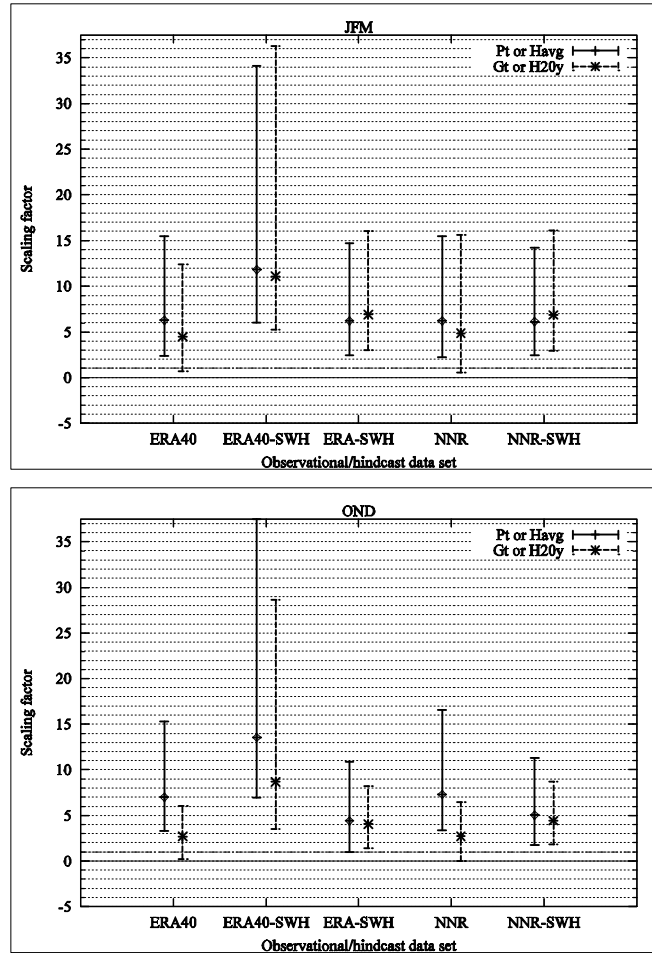
Figure 4. The scaling factors ($\hat{b}$) in the regressions of the 1958-1999 trend patterns of the seasonal mean SLP anomalies P_t, seasonal anomalies of squared SLP gradients G_t, and seasonal means and 20-yr return values of SWH (H_{avg} and H_{20y}), separately, on the relevant multi-model mean of simulated trend patterns. The labels "ERA40" and "NNR" denote the results of detection on P_t and G_t as derived from ERA40 and NNR, respectively. While the label "ERA40-SWH" denotes the results of detection on the original ERA40 SWH data, "ERA-SWH" and "NNR-SWH" denote those on the SWH hindcasts using as predictors P_t and G_t as derived from ERA40 and NNR, respectively.

However, the associated 5-95% uncertainty ranges on b do not include unity in most cases (especially for the seasonal mean quantities P_t or H_{avg}; see Table 2 and Fig. 4), which suggests that the models significantly underestimate the magnitude of the response of the ocean wave heights and atmospheric storminess to increases in greenhouse gases and sulphate aerosols (assuming the observed trends are not systematically overestimated in the ERA40 or NNR data). The residual h was found to be consistent with the corresponding inter-integration variability for

all winter cases, but only for half of the fall cases. Specifically, in fall, the climate models were found to underestimate the internal variability in P_t of both ERA40 and NNR, in G_t of ERA40, and in H_{avg} of the ERA40 or NNR hindcast (see Table 2). Such an underestimate leads to conservative detection conclusions.

3. Conclusions

In this study, work on detection of human influence on North Atlantic ocean wave heights and atmospheric storminess is performed, based on multiple climate models simulations of human-induced climate change and statistical simulations of the corresponding changes in ocean wave heights for the cold seasons of 1958-1999. Two global reanalyses, ERA40 and NNR, are used as proxy of observations of the atmosphere and ocean wave heights (both seasonal means and extremes).

The results suggest that anthropogenic greenhouse gases and sulphate aerosols have had a detectable influence on North Atlantic ocean wave heights and atmospheric storminess in the cold seasons (especially winter). The observed 1958-1999 trend patterns of ocean wave heights and atmospheric storminess are characterized by an upward trend in the high-latitudes (especially the northeast North Atlantic in winter) with a downward trend to the south, which were found to contain a detectable response to the anthropogenic forcing. However, the climate models were found to significantly underestimate the magnitude of the response in general, while these models also underestimate the internal variability in the fall season.

References

Allen, M. R., and P. A. Stott (2003), Estimating signal amplitudes in optimal fingerprinting, part I: Theory, *Clim. Dyn*., 21, 477-491.

Bacon, S. and D. J. T. Carter (1991), Wave climate changes in the North Atlantic and North Sea, *Int. J. Climatol.,* 11, 545-558.

Caires, S., A. Sterl, G. Komen, V. Swail (2004), The Web-based KNMI/ERA-40 global wave climatology atlas, WMO Bulletin, 53(2), 142-146

Gillett, N. P., A. J. Weaver, F. W. Zwiers, and M. D. Flannigan (2004), Detecting the effect of climate change on Canadian forest fires, *Geophys. Res. Lett.*, 31, L18211, doi:10.1029/2004GL020876.

Kalnay, E., M. Kanamitsu, R. Kistler, W. Collins, D. Deaven, L. Gandin, M. Iredell, S. Saha, G. White, J. Woollen, Y. Zhu, M. Chelliah, W. Ebisuzaki, W. Higgins, J. Janowiak, K. C. Mo, C. Ropelewski, J. Wang, A. Leetmaa, R. Reynolds, R. Jenne, and D. Joseph (1996), The NCEP/NCAR 40-year reanalysis project. *Bull. Amer. Meteor. Soc.*, 77, 437-471.

Kistler, R., and co-authors (2001), The NCEP-NCAR 50-year reanalysis: Monthly means CD-Rom and documentation. *Bull. Amer. Meteor. Soc.*, 82, 247-267.

Uppala, S. M., and co-authors (2005), The ERA-40 re-analysis, Quart. *J. Roy. Meteor. Soc.*, 131, 2961-3012.

WASA Group (1998), Changing Waves and Storms in the Northeast Atlantic? *Bull. Amer. Meteor. Soc*, 79, 741-760.

Wang, X. L., V. R. Swail and F. W. Zwiers (2006), Climatology and changes of extra-tropical cyclone activity: Comparison of ERA-40 with NCEP/NCAR Reanalysis for 1958-2001, *J. Clim.*, 19, 3145-3166. doi: 10.1175/JCLI3781.1.

Wang, X. L. and V. R. Swail (2006a), Historical and possible future changes of wave heights in northern hemisphere oceans, *Atmosphere Ocean Interactions - Volume 2* [Perrie, W. (ed.)], Advances in Fluid Mechanics Series Vol 39, Wessex Institute of Technology Press, Southampton, UK, 240pp.

Wang, X. L. and V. R. Swail (2006b), Climate change signal and uncertainty in projections of ocean wave heights, *Clim. Dyn*.,26, 109-126, doi:10.1007/s00382-005-0080-x.

Wang, X. L. and V. R. Swail (2002), Trends of Atlantic wave extremes as simulated in a 40-year wave hindcast using kinematically reanalyzed wind fields, *J. Clim.*, 15, 1020-1035.

Wang, X. L. and V. R. Swail (2001), Changes of extreme wave heights in northern hemisphere oceans and related atmospheric circulation regimes, *J. Clim.*, 14, 2204-2221.